A porous circulation model of the human brain for in silico clinical trials in ischaemic stroke

Józsa, T.I.; Padmos, R.M.; Samuels, N.; El-Bouri, W.K.; Hoekstra, A.G.; Payne, S.J.

DOI
10.1098/rsfs.2019.0127

Publication date
2021

Document Version
Final published version

Published in
Interface Focus

INTERFACE FOCUS

royalsocietypublishing.org/journal/rsfs

Research

Cite this article: Józsa TI, Padmos RM, Samuels N, El-Bouri WK, Hoekstra AG, Payne SJ. 2021 A porous circulation model of the human brain for *in silico* clinical trials in ischaemic stroke. *Interface Focus* **11**: 20190127.
http://dx.doi.org/10.1098/rsfs.2019.0127

Accepted: 23 September 2020

One contribution of 11 to a theme issue 'Computational biomedicine. Part II: organs and systems'.

Subject Areas:
biomedical engineering, biomechanics

Keywords:
organ-scale model, human brain, finite-element method, ischaemic stroke, multi-compartment porous model

Author for correspondence:
T. I. Józsa
e-mail: tamas.jozsa@eng.ox.ac.uk

A porous circulation model of the human brain for *in silico* clinical trials in ischaemic stroke

T. I. Józsa[1], R. M. Padmos[2], N. Samuels[3], W. K. El-Bouri[1], A. G. Hoekstra[2] and S. J. Payne[1]

[1]Institute of Biomedical Engineering, Department of Engineering Science, University of Oxford, Parks Road, Oxford OX1 3PJ, UK
[2]Computational Science Laboratory, Institute for Informatics, Faculty of Science, University of Amsterdam, Science Park 904, Amsterdam 1098 XH, The Netherlands
[3]Department of Radiology and Nuclear Medicine, Erasmus MC, University Medical Center, Rotterdam 3015 GD, The Netherlands

TIJ, 0000-0002-5082-0299; RMP, 0000-0001-7253-240X; NS, 0000-0002-6846-9695; WKE-B, 0000-0002-2732-5927; AGH, 0000-0002-3955-2449; SJP, 0000-0003-1156-2810

The advancement of ischaemic stroke treatment relies on resource-intensive experiments and clinical trials. In order to improve ischaemic stroke treatments, such as thrombolysis and thrombectomy, we target the development of computational tools for *in silico* trials which can partially replace these animal and human experiments with fast simulations. This study proposes a model that will serve as part of a predictive unit within an *in silico* clinical trial estimating patient outcome as a function of treatment. In particular, the present work aims at the development and evaluation of an organ-scale microcirculation model of the human brain for perfusion prediction. The model relies on a three-compartment porous continuum approach. Firstly, a fast and robust method is established to compute the anisotropic permeability tensors representing arterioles and venules. Secondly, vessel encoded arterial spin labelling magnetic resonance imaging and clustering are employed to create an anatomically accurate mapping between the microcirculation and large arteries by identifying superficial perfusion territories. Thirdly, the parameter space of the problem is reduced by analysing the governing equations and experimental data. Fourthly, a parameter optimization is conducted. Finally, simulations are performed with the tuned model to obtain perfusion maps corresponding to an open and an occluded (ischaemic stroke) scenario. The perfusion map in the occluded vessel scenario shows promising qualitative agreement with computed tomography images of a patient with ischaemic stroke caused by large vessel occlusion. The results highlight that in the case of vessel occlusion (i) identifying perfusion territories is essential to capture the location and extent of underperfused regions and (ii) anisotropic permeability tensors are required to give quantitatively realistic estimation of perfusion change. In the future, the model will be thoroughly validated against experiments.

1. Introduction

In recent decades, ischaemic stroke treatment has been revolutionized by thrombolysis (the dissolving of blood clot) [1] and thrombectomy (the mechanical removal of clot) [2,3]. Consequently, the functional outcome and survival rate of ischaemic stroke patients has increased [4,5]. When successful, both thrombolysis and thrombectomy restore blood flow in the previously blocked vessels (recanalization). However, it has been reported that even after recanalization, blood flow to the tissue downstream to the occluded artery (perfusion) is often not or only partially recovered and hence brain tissue loss continues [1,6]. The post-treatment mortality rate of patients who suffered from an ischaemic stroke is still relatively high [7]. In addition, a substantial proportion of the

THE ROYAL SOCIETY PUBLISHING

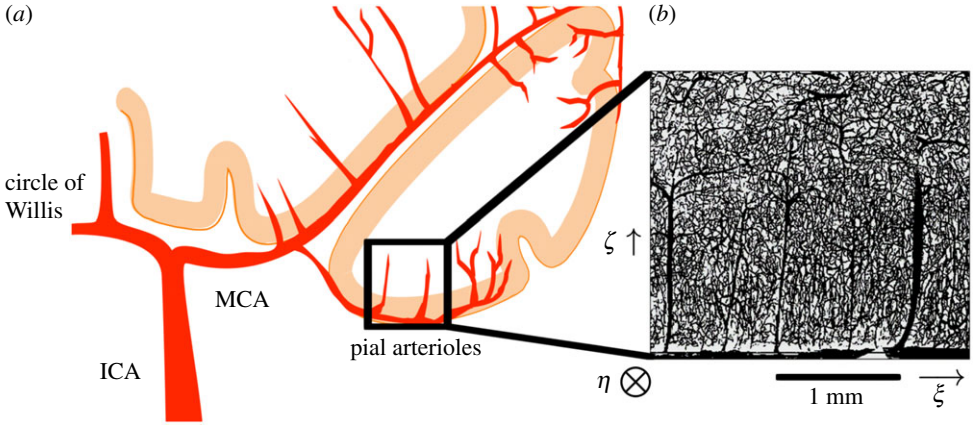

Figure 1. Structure of the brain vasculature: (*a*) schematic drawing of the large arteries including the internal carotid artery (ICA) and the middle cerebral artery (MCA). Adapted from the work of Iadecola [17]. (*b*) structure of the human cerebral mircovasculature visualized with india ink under confocal laser microscopy. Modified with permission from Iadecola [17] (*a*) and Cassot *et al.* [18] (*b*). The reference coordinate system (ξ, η, ζ) is shown in (*b*).

survivors (25–74%) suffer from a severe loss of congnitive function [8]. Taking care of functionally dependent patients imposes a heavy burden on society, both economically and mentally [7].

Regarding the poor outcome of ischaemic stroke patients, it is recognized that certain mechanisms can limit perfusion restoration. For instance, recanalization techniques are accompanied by the risk of thrombus fragmentation leading to downstream occlsusions [9]. It has been hypothesized that when emboli reach the microcirculation, they cause micro-occlusions, and hence prevent reperfusion [10]. Another important mechanism is cerebral oedema, during which swelling of the brain deforms the tissue and alters blood pressure [11]. In order to maximize the positive outcome of treatments, such hypotheses have to be carefully investigated and counteracting interventions have to be worked out. The advancement and further development of related drugs and devices rely on resource-intensive and time-consuming pre-clinical animal experiments and clinical studies. Unfortunately, the success rate of treatment that passes pre-clinical testing is low because the human brain behaves very differently from cell cultures or animal brains [12].

The INSIST (*IN Silico* clinical trials for treatment of acute Ischaemic STroke) consortium (https://www.insist-h2020.eu) set out to accelerate the advancement of human ischaemic stroke treatments by introducing *in silico* clinical trials which mitigate the need for resource-intensive experiments [13]. INSIST promotes the application of computational methods for pharmacology and medical device development, which aligns with the ambitions of the virtual physiological human (VPH) initiative [14]. This study contributes to INSIST and the VPH by developing a cerebral microcirculation model for the entire human brain, which is capable of predicting perfusion before and after an ischaemic stroke. This model will be coupled to a one-dimensional blood flow simulator governing blood flow in arteries supplying blood to the pial surface [15,16]. The role of the resulting organ-scale cerebral blood flow model in the *in silico* clinical trial will be to evaluate the impact of stroke treatment (thrombectomy or thrombolysis) on tissue perfusion. Furthermore, the model will provide input to other models which describe oxygen transport and infarct progression in the brain. The envisioned software suite will predict the outcome of ischaemic stroke treatment on a population level, provide guidance for objective clinical decision making, and lead to further drug and medical device development.

Progress in the mathematical and computational modelling of the cerebral circulation is complicated by the multi-scale nature of the flow and related transport processes. The diameter of blood vessels stretches from approximately 5 mm to 5 µm, being characteristic of the internal carotid artery and the capillaries, depicted in figure 1*a*,*b*, respectively. Cortical columns (with volumes of a few cubic millimetres) have been modelled by treating the capillary bed as a porous medium [19] and representing the connecting arterioles and venules as a one-dimensional vessel network [20,21]. Scaling such models to the entire brain is computationally resource intensive, because it requires capturing the flow in the corresponding large networks of arterioles and venules. Nevertheless, with simplifications regarding the vessel networks, this approach has been successfully employed to investigate the temperature regulation of the human brain [22]. To overcome difficulties originating from the large networks, a two-compartment porous continuum model has been implemented for the human brain [23] where the arteriole and venule compartments include the majority of the small vessels. These models are reminiscent of heart perfusion models [24–26].

The present study sets out to investigate the capabilities of porous continuum models in terms of estimating the perfusion changes in various brain territories as a result of a large intracranial vessel occlusion. To this end, we aim to improve the recently introduced organ-scale cerebral microcirculation models [22,23]. As shown in figure 1*a*,*b*, the descending arterioles (and ascending venules) originating from the pial vessels are oriented perpendicularly to the cortical surface. The continuum representation of such networks requires anisotropic permeability fields [24–26] which have been disregarded in previous studies for simplicity [22,23,27]. It has been demonstrated that capturing such spatial variation in the properties of the continuum models plays an important role in the description of organ-scale physiological processes [28,29].

Firstly, a robust algorithm will be presented which accounts for the anisotropy of the human microcirculation due to penetrating vessels. Thanks to brain atlases [30] and medical imaging technologies, such as vessel encoded arterial spin labelling magnetic resonance imaging (VE-ASL MRI) [31,32], it is now well known that large vessels supply specific

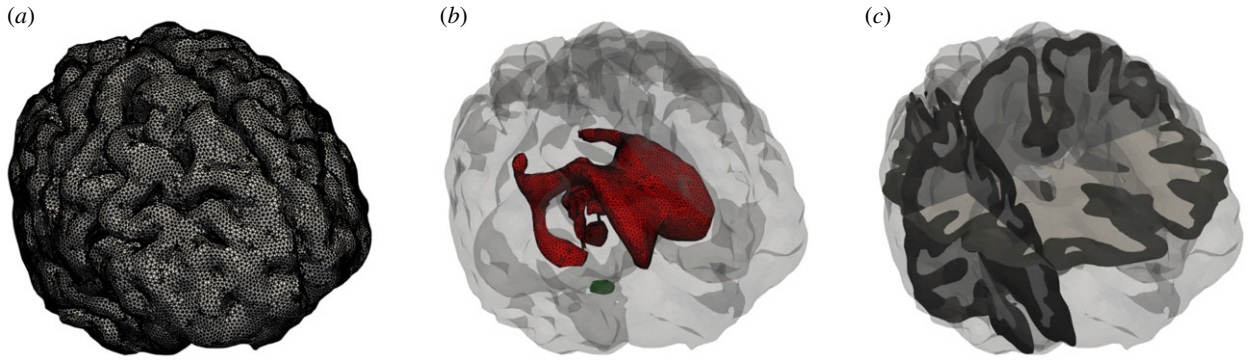

Figure 2. Computational domain and mesh: (*a*) the pial surface; (*b*) ventricles (red) and the cut-plane of the brainstem (green); (*c*) subdomains including grey and white matters visualized along a coronal, a sagittal and a transverse plane.

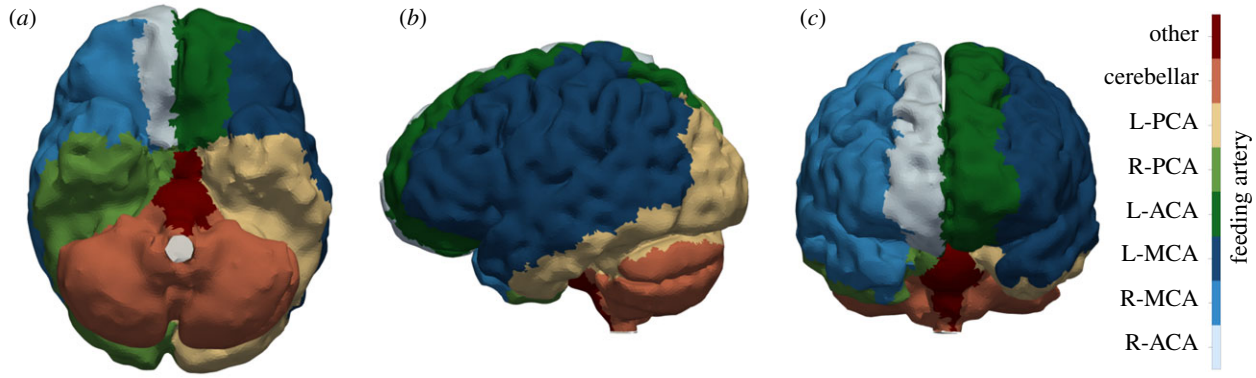

Figure 3. Superficial perfusion territories of large arteries projected onto the brain surface using the algorithm presented in [15,16] and VE-ASL MRI images [43]: (*a*) transverse view; (*b*) sagittal view; (*c*) coronal view. Territories corresponding to the left and right (L and R) hemispheres are labelled separately. Surface regions are coloured based on the feeding arteries using the following acronyms: anterior cerebral artery (ACA), middle cerebral artery (MCA), posterior cerebral artery (PCA).

brain regions. Modelling the connections between large vessels and their corresponding territories is crucial to predict the brain regions that are influenced by large vessel occlusion. In former studies [22,23], the volume sources that coupled the one-dimensional networks and the porous continuum were not designed to incorporate these features. Secondly, a mapping will be introduced between the micro and macro scales based on VE-ASL MRI. Thirdly, we will parametrize the resulting porous continuum model and conduct optimization to determine the unknown parameters. Finally, for the first time, simulations will be reported which are capable of producing realistic perfusion maps in healthy and occluded (ischaemic stroke) scenarios.

2. Methods

When considering organ-scale perfusion models, it is becoming common practice to use one-dimensional network models (e.g. [33–37]) for large arteries and multi-compartment porous continuum models for the microcirculation [22–26]. The microcirculation model proposed here builds on the same principles.

2.1. Computational domain and mesh

The computational domain (Ω) is a patient-specific human brain used in multiple recent studies [29,38,39]. The bounding surface regions ($\partial\Omega$) include a transverse cut-plane of the brainstem Γ_{BS}, the ventricles Γ_V and the pial surface Γ_P so that $\partial\Omega = \Gamma_{\mathrm{BS}} \cup \Gamma_V \cup \Gamma_P$. These surface regions are depicted in figure 2*a*,*b*. Grey matter (Ω_{G}) and white matter (Ω_{W}) are visible along a transverse, a coronal and a sagittal plane in figure 2*c*. Our investigations are restricted to these two subdomains, therefore $\Omega = \Omega_{\mathrm{G}} \cup \Omega_{\mathrm{W}}$. The geometry is discretized on a tetrahedral mesh using Tetgen [40]. The mesh depicted in figure 2 includes 1 042 301 elements.

The boundary region associated with the pial surface (figure 2*a*) is subdivided into eight perfusion territories corresponding to major feeding arteries which have been identified with VE-ASL MRI [31,32,41–43]. To this end, the same clustering algorithm is used as in our preliminary study [44] as detailed in [15,16]. In the future, subdividing the pial surface into more sections will enable us to establish a feedback between the porous microcirculation model and a one-dimensional network model [15,16] by the repeated refreshment of the boundary conditions. Each perfusion territory corresponds to a major feeding artery of the brain. These territories are identified based on VE-ASL MRI images [43]. Thereafter, the surface region that is perfused, for instance, by the right middle cerebral artery (R-MCA) is denoted as $\Gamma_{\text{R-MCA}}$. This approach leads to an anatomically accurate coupling by ensuring that blood arrives to the brain tissue through specific cortical surface regions as shown in figure 3*a*–*c*.

2.2. Governing equations and boundary conditions

The governing equations describing three porous compartments [24–26] are

$$\nabla \cdot (\boldsymbol{K_a} \nabla p_a) - \beta_{\mathrm{ac}}(p_a - p_c) = 0; \tag{2.1a}$$

$$\nabla \cdot (\boldsymbol{K_c} \nabla p_c) + \beta_{\mathrm{ac}}(p_a - p_c) - \beta_{\mathrm{cv}}(p_c - p_v) = 0; \tag{2.1b}$$

$$\nabla \cdot (\boldsymbol{K_v} \nabla p_v) + \beta_{\mathrm{cv}}(p_c - p_v) = 0. \tag{2.1c}$$

Here, p_a, p_c and p_v are the Darcy pressures corresponding to the arteriole, capillary and venule compartments, respectively. $\boldsymbol{K_i}$ is the permeability tensor of compartment i, whereas β_{ij} denotes

the coupling coefficients between compartments i and j. It is worth mentioning that a similar two-compartment (arteriole and venule) brain perfusion model has been reported recently [23]. Here, a three-compartment model is proposed because some relevant physiological and biochemical processes are restricted to certain length scales. For instance, oxygen exchange through the blood brain barrier is most intensive in the capillary compartment. Furthermore, cerebral autoregulation mechanisms are different in arterioles and capillaries and seem to be absent in venules [45–47].

The boundary conditions imposed with equation (2.1) are as follows. Flow through the transverse cut-plane of the brainstem and the ventricles is zero in every compartment. Using $\boldsymbol{n}$ as the outward-pointing normal unit vector corresponding to the boundary surface, this Neumann boundary condition reads as

$$\boldsymbol{K}_i \nabla p_i \cdot \boldsymbol{n} = 0 \quad \text{on } \Gamma_{\text{BS}} \text{ and } \Gamma_V. \tag{2.2}$$

Flow through the pial surface in the capillary compartment is zero

$$\boldsymbol{K}_c \nabla p_c \cdot \boldsymbol{n} = 0 \quad \text{on } \Gamma_P. \tag{2.3}$$

The zero level of pressure can be selected freely because of the incompressible fluid flow model. By setting the zero level of pressure on the pial surface in the venous compartment, the value of the venous pressure is eliminated from the model

$$p_v = 0 \quad \text{on } \Gamma_P. \tag{2.4}$$

In the healthy scenario, the pressure on the pial surface in the arteriole compartment is the diastolic pressure (p_{dia})

$$p_a = p_{\text{dia}} \quad \text{on } \Gamma_P. \tag{2.5}$$

To account for totally occluded scenarios, blood flow through the perfusion territory of an occluded vessel is set to zero whereas surface pressure is assumed to remain constant in other regions. Accordingly, the mixed boundary conditions corresponding, for instance, to a R-MCA occlusion become

$$\frac{\partial p_a}{\partial \boldsymbol{n}} = 0 \quad \text{on } \Gamma_{\text{R-MCA}} \tag{2.6a}$$

and

$$p_a = p_{\text{dia}} \quad \text{on } \Gamma_P \backslash \Gamma_{\text{R-MCA}}. \tag{2.6b}$$

2.3. Model parameters

The haemodynamics model governed by equation (2.1) includes 31 parameters: the coupling coefficients in grey (β^G_{ac} and β^G_{cv}) and white matters (β^W_{ac} and β^W_{cv}), and the 27 components of the permeability tensors of each compartment ($\boldsymbol{K}_a$, $\boldsymbol{K}_c$, $\boldsymbol{K}_v$). The permeability tensors and the coupling coefficients of the porous model need to represent the complex structure of the microvasculture with strong preferences regarding arteriole and venule vessel orientation as shown in figure 1. Therefore, the components of $\boldsymbol{K}_a$ and $\boldsymbol{K}_v$ are space-dependent functions. However, as the structure of the microvasculature in the mammalian brain changes with increasing cortical depth [48] and it is likely to exhibit territorial dependence, these properties are neglected here due to the lack of data. Characterizing such spatial variations remains an outstanding challenge for the modelling and the experimental communities.

Penetrating vessels, including descending arterioles (DAs) and ascending veins (AVs), in the cortex tend to be aligned normal to the pial surface. Consequently, the permeability tensors of the arteriole and venule compartments are similar but anisotropic and inhomogeneous. On the contrary, it has been reported that the permeability tensor of the capillary compartment is approximately isotropic [19,49,50]. Based on statistically accurate capillary network simulations [19,51], the capillary permeability in the grey matter can be described by a single scalar: $k_c = 4.28 \times 10^{-4}$ [mm^3 s kg^{-1}]. For simplicity, we use some assumptions first proposed by [23]: (i) the permeabilities are the same in grey and white matters and (ii) $\boldsymbol{K}_v = 2\boldsymbol{K}_a$. In addition, (iii) the ratio of the grey and white matter coupling coefficients is assumed to be constant

$$C_\beta = \frac{\beta^G}{\beta^W} = \frac{\beta^G_{\text{ac}}}{\beta^W_{\text{ac}}} = \frac{\beta^G_{\text{cv}}}{\beta^W_{\text{cv}}}. \tag{2.7}$$

Thereafter, the model is determined by twelve parameters: β^G_{ac}, β^G_{cv}, C_β and $\boldsymbol{K}_a$.

2.3.1. Permeability tensors

Permeabilities are characterized in a reference Cartesian coordinate system defined by ξ, η, ζ corresponding to a cortical column as shown in figure 1*b*. The $\boldsymbol{e}_{\text{ref}} = [0, 0, 1]$ unit vector defined in the reference coordinate system is parallel to the axes of the penetrating vessels (figure 1*b*). The arteriole and the venule compartments encapsulate the zeroth-order penetrating vessel branches. These major penetrating branches in a cortical column can be imagined as a 'vessel bundle' supporting flow only in the ζ direction. For this reason, we assume that the arteriole and venule permeabilities in the reference coordinate system are

$$\boldsymbol{K}^{\text{ref}}_a = \begin{bmatrix} 0 & 0 & 0 \\ 0 & 0 & 0 \\ 0 & 0 & k_a \end{bmatrix} \quad \text{and} \quad \boldsymbol{K}^{\text{ref}}_v = \begin{bmatrix} 0 & 0 & 0 \\ 0 & 0 & 0 \\ 0 & 0 & k_v \end{bmatrix}. \tag{2.8}$$

In this formulation, every higher order arteriole and venule side branch is lumped into a conductance represented by the coupling coefficients.

This approach includes numerous simplifications but it has three advantages. Firstly, the permeability of a 'vessel bundle' with laminar flow within (k_{vb}) can be estimated as

$$k_a \approx k_{vb} = \frac{n_v D^4 \pi}{128 \mu_b A_{\text{ref}}}. \tag{2.9}$$

Here, D is the characteristic diameter of the vessels and n_v is the number of vessels corresponding to a reference cortical surface area A_{ref}. The *in vitro* dynamic viscosity of blood (μ_b) depends on the diameter and the haematocrit as described in [52]. Assuming a constant discharge haematocrit of 45%, a mean diameter in the range of $D = 50-90\,\mu$m [49,53] with $n_v = 8$ pial arteries per $A_{\text{ref}} = 1$ mm^2 [20,54], the arterial permeability can be estimated from equation (2.9) resulting in $k_a/k_c = 1000–10\,000$. The final value of k_a is optimized with an initial guess within this range. This optimization is presented in §3.1.

Secondly, in the reference coordinate system the arteriole and venule permeability tensors have only one constant non-zero element (instead of space-dependent functions). Thirdly, once a permeability tensor is determined in a reference coordinate system ($\boldsymbol{K}_i^{\text{ref}}$) with a given reference direction ($\boldsymbol{e}_{\text{ref}}$), the permeability tensor (function) $\boldsymbol{K}_i$ can be computed. The corresponding transformation detailed in appendix A requires a unit vector representing the local characteristic direction ($\boldsymbol{e}_{\text{local}}$). To date, studies on porous modelling of the human brain [22,23,27] assumed isotropic and homogeneous permeabilities because $\boldsymbol{e}_{\text{local}}$ could not be obtained. To overcome this problem, a computational approach is proposed that relies solely on the geometry of the domain of interest.

The local brain tissue thickness is the length of a curve connecting a point on the ventricular surface (Γ_V) to a point on the pial surface (Γ_P). The normalized thickness (t) increases from zero to one as a point moves from Γ_V to Γ_P along the curve defining the thickness. The normalized thickness can be computed by solving the Poisson equation

$$\nabla^2 t = 0, \tag{2.10}$$

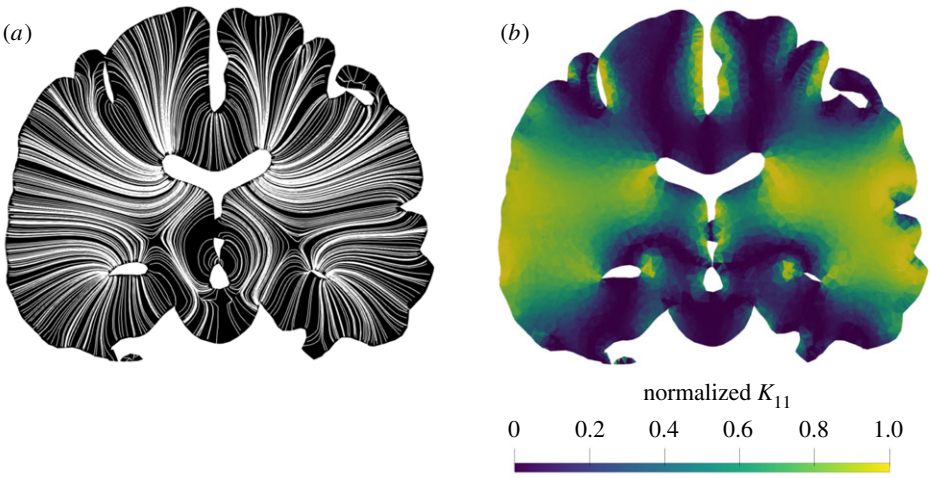

Figure 4. Tangent lines of the $\boldsymbol{e}_{\text{local}}$ vector field representing the local characteristic direction of the penetrating vessels (*a*). The first diagonal component of the arteriole or the venule permeability tensor adjusted using the $\boldsymbol{e}_{\text{local}}$ field (*b*).

with $t = 0$ on Γ_V, $t = 1$ on Γ_P and $\nabla t \cdot \boldsymbol{n} = 0$ on Γ_{BS}. Assuming that penetrating vessels grow from the pial surface by following the fastest descent thorough the brain tissue, the unit vector corresponding to their local characteristic direction is given as

$$\boldsymbol{e}_{\text{local}} = \frac{\nabla t}{|\nabla t|}. \tag{2.11}$$

In figure 4*a*, the $\boldsymbol{e}_{\text{local}}$ vector field is visualized by the corresponding tangent lines equivalent of the curves defining brain tissue thickness. It is hypothesized that vessels follow these curves which highlight the least resistant path through the brain tissue without being entangled. This assumption overlaps with microscopical observations of the human microcirculation about arterioles and venules penetrating perpendicularly to the cortical surface [18,49]. The permeability tensors of the arteriole and venule compartments are rotated to support blood flow only parallel to $\boldsymbol{e}_{\text{local}}$. The first diagonal component of the normalized arteriole permeability tensor is depicted in figure 4*b*. High values of K_{11} indicate regions where blood flow in the arterioles and the venules is supported primarily in the lateral direction. Where K_{11} is relatively low, blood flow occurs mostly along the distal–proximal and the anterior–posterior directions.

2.3.2. Coupling coefficients

The coupling coefficients are tuned to account for the side branches of the penetrating arterioles and venules. These side branches are referred to as PreCapillaries (PrC) and PostCapillaries (PoC) associated with β_{ac} and β_{cv}, respectively. In order to estimate these parameters, the volume-averaged pressure fields are linked to the coupling coefficients.

Integrating equations (2.1*a*)–(2.1*c*) over Ω_G, applying the divergence theorem, and dividing by the total volume of the grey matter (V_G) leads to the following algebraic equation set:

$$-\frac{Q_a^G}{V_G} - \beta_{ac}^G(\langle p_a\rangle^G - \langle p_c\rangle^G) = 0; \tag{2.12a}$$

$$-\frac{Q_c^G}{V_G} + \beta_{ac}^G(\langle p_a\rangle^G - \langle p_c\rangle^G) - \beta_{cv}^G(\langle p_c\rangle^G - \langle p_v\rangle^G) = 0; \tag{2.12b}$$

$$-\frac{Q_v^G}{V_G} + \beta_{cv}^G(\langle p_c\rangle - \langle p_v\rangle^G) = 0. \tag{2.12c}$$

Here, the angle brackets denote volume-averaged quantities so that $\langle p_i\rangle^G$ is the average Darcy pressures in the grey matter in compartment i. Furthermore, Q_i^G is the volumetric flow rate through the surface bounding the grey matter in compartment i, defined as

$$Q_i^G = -\iint_{\Gamma_G} \boldsymbol{K}_i \nabla p_i \cdot \mathrm{d}\boldsymbol{A}. \tag{2.13}$$

In the above expression Γ_G and $\boldsymbol{A}$ symbolize the surface bounding the grey matter and the corresponding area vector, respectively.

Given that $k_a/k_c = 1000-10\,000$, as estimated in §2.3.1, Q_c^G/V_G is negligible compared to Q_a^G/V_G and Q_v^G/V_G. According to the imposed boundary conditions, equations (2.2) and (2.3), $Q_c^G/V_G \approx 0$ can be assumed which indicates that blood flow in the capillaries through the interface of grey and white matter is comparatively low. This assumption has been used previously in blood flow simulations of cortical columns [19,21]. Based on equation (2.12), it thus follows that grey matter perfusion is

$$F^G = -\frac{Q_a^G}{V_G} = \beta_{ac}^G(\langle p_a\rangle^G - \langle p_c\rangle^G) = \beta_{cv}^G(\langle p_c\rangle^G - \langle p_v\rangle^G). \tag{2.14}$$

In addition, it can be concluded that the ratio of the arteriole–capillary (β_{ac}) and the capillary–venule (β_{cv}) coupling coefficients is related to the volume-averaged pressure drops as

$$\frac{\beta_{ac}^G}{\beta_{cv}^G} = \frac{\langle p_c\rangle^G - \langle p_v\rangle^G}{\langle p_a\rangle^G - \langle p_c\rangle^G}. \tag{2.15}$$

Therefore, the average perfusion and inter-compartment pressure drops in the grey matter uniquely determine the coupling coefficients β_{ac}^G and β_{cv}^G.

In order to calculate the coupling coefficient in the grey matter, perfusion is calculated from cerebral blood flow set to $Q^{\text{brain}} = 600$ [ml min^{-1}] [55]. The total volume of the brain model is $V_{\text{brain}} = 1390$ [ml] which leads to a physiologically realistic brain perfusion $F^{\text{brain}} \approx 43$ [(ml blood) min^{-1} (100 ml tissue)$^{-1}$]. The mean ratio of grey and white matter perfusion is $F^G/F^W = 2.7$ [56]. With the grey and white matter volumes given ($V^G = 894$ and $V^W = 496$ [ml]), grey and white matter perfusion values are $F^G \approx 56$ and $F^W \approx 21$ [ml min^{-1} (100 ml)$^{-1}$] respectively. The brain volume [57] and perfusion values [32,42,56] are in good agreement with the literature.

Pressure measurements in the human microcirculation are not available but experiments have been reported in the rat brain [58,59]. Based on the summary of these experiments provided by Schmid *et al.* [48], some normalized experimental results are shown in figure 5*a*. $\beta_{cv}/\beta_{ac} = 3.5$ is inferred from the ratio of the average pressure drop in each compartment of the rat brain. It is worth mentioning that simulations of the rat brain indicate significant variation of the pressure ratios in different cortical layers [48]. Finally, the diastolic pressure in the human brain is set to $p_{\text{dia}} = 75$ mmHg $\approx 10^4$ Pa. (This value is relative to the venous pressure selected as the zero level of the pressure.) According to the calculated grey matter perfusion, the pressure ratios visualized in figure 5*a* and the diastolic pressure value, the coupling coefficients in grey matter are

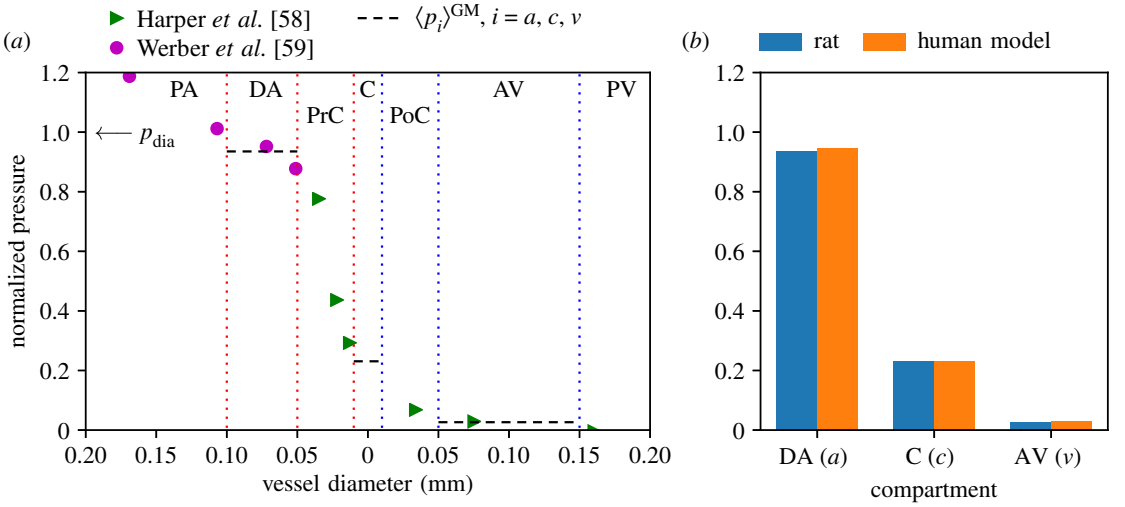

Figure 5. Normalized pressure as a function of the vessel diameter in the grey matter of the rat brain (*a*). The diastolic pressure is used for normalization. The dotted lines represent theoretical boundaries between the pial arteries (PA), descending arterioles (DA), precapillaries (PrC), capillaries (C), post capillaries (PoC), ascending venules (AV) and pial veins (PV). The dashed lines represent the hypothetical average pressure values in each compartment. Average pressure in the arteriole, capillary and the venule compartments in the grey matter of the rat brain and the present virtual human brain (*b*).

$\beta^G_{ac} = 1.326 \times 10^{-6}$ and $\beta^G_{cv} = 4.641 \times 10^{-6}$ [$\mathrm{Pa^{-1}\,s^{-1}}$]. Figure 5*b* demonstrates that with these coupling coefficients, the normalized inter-compartment pressure drop of the human brain model is similar to that of the rat brain. Finally, $C_\beta = \beta^G/\beta^W$ can be estimated analytically by rewriting equation (2.14) for the white matter and assuming that the inter-compartment pressure drop in white matter is the same as in grey matter: $F^G/F^W = \beta^G/\beta^W = 2.7$.

2.4. Numerical procedure

It has been demonstrated that the finite-element method can be used efficiently to model complex physical problems in human organs [28,60–64], including fluid flow and solid deformation in the human brain [11]. For this reason, the governing partial differential equations are solved numerically using Python with a high-performance open source finite-element library, FEniCS [65,66]. The weak form of equation (2.1) is available in [24] and in appendix B. The equation set is solved in a mixed space covering the full system. The pressure in each compartment (p_i) is discretized using piecewise linear Lagrange (P_1) elements. (The 'periodic table' of finite elements can be found in [67].) The permeabilities ($\boldsymbol{K}_i$) and the coupling coefficients (β_{ij}) are represented in (discontinuous) piecewise constant (dP_0) tensor and scalar function spaces, respectively. This helps to capture the sharp change in the model parameters between the grey and white matters.

The *a* scalar in the Poisson equation (2.10) is stored in second-order piecewise polynomial Lagrange (P_2) elements. Therefore, $\boldsymbol{e}_{local}$ in equation (2.11) has to be projected from P_1 to dP_0 elements before it is used for the coordinate transformation of $\boldsymbol{K}_i^{ref}$. Finally, tissue perfusion $F = \beta_{ac}(p_a - p_c)$ is computed in dP_0 elements. The resulting linear equation systems are solved iteratively using the biconjugate gradient stabilized method [68]. Pressure field computation is speeded up with an algebraic multigrid preconditioner [69]. Adjusting the permeability field and computing the pressure and perfusion fields for the healthy and occluded scenarios take approximately 5 min using a single core on a modern desktop equipped with an Intel Xeon E-2146G processor. Exploiting the native message passing interface implementation of FEniCS and running the simulations with two and four cores reduce the wall time to approximately 3 and 2 min, respectively.

3. Results and discussion

3.1. Parameter optimization

It turns out that without the simplifications listed in §2, it is challenging to pose an optimization problem with well-distinguished global or local minimum for the complete set of 31 parameters. For this reason, the parameter space of the imposed problem is reduced significantly according to §§2.3.1 and 2.3.2 and the remaining parameters are optimized.

The optimization goal is to obtain physiologically accurate average perfusion values for the grey and white matters, hence the cost function (J) to be minimized is

$$J = (F^G - F^G_{target})^2 + (F^W - F^W_{target})^2 + J_{penalty}. \qquad (3.1)$$

The target values are calculated as detailed in §2.3.2 and set to $F^G_{target} \approx 56$ and $F^W_{target} \approx 21$ [(ml blood) $\mathrm{min^{-1}}$ (100 ml tissue)$^{-1}$]. Furthermore, a penalty term ($J_{penalty}$) has been added to restrict the minimum and maximum perfusion values

$$\begin{aligned} J_{penalty} = {} & H(F_{min,target} - F_{min}) \cdot (F_{min} - F_{min,target})^2 \\ & + H(F_{max} - F_{max,target}) \cdot (F_{max} - F_{max,target})^2. \end{aligned} \qquad (3.2)$$

Here, H is the Heaviside function resulting in a non-zero $J_{penalty}$ only if the extrema are out of the $F_{min,target} = 10$ and the $F_{max,target} = 80$ [(ml blood) $\mathrm{min^{-1}}$ (100 ml tissue)$^{-1}$] range.

The two remaining parameters are defined as

$$\frac{k_a}{k_c} = 10^p \quad \text{and} \quad C_\beta = \frac{\beta^G}{\beta^W} = 10^q, \qquad (3.3)$$

to restrict the search for positive values. Finally, the two-dimensional optimization problem can be phrased as

$$\min[J(p, q)] \text{ in } \; p \in [-\infty, \infty] \quad \text{and } q \in [-\infty, \infty]. \qquad (3.4)$$

The parameters are initialized randomly within the $p \in [3, 4]$ and $q \in [0, 1]$ intervals. The bounding values are estimated according to §§2.3.1 and 2.3.2. To find the global minimum of J, the BFGS [70] and the Nelder–Mead [71] methods are employed. Whereas the BFGS method relies on computing

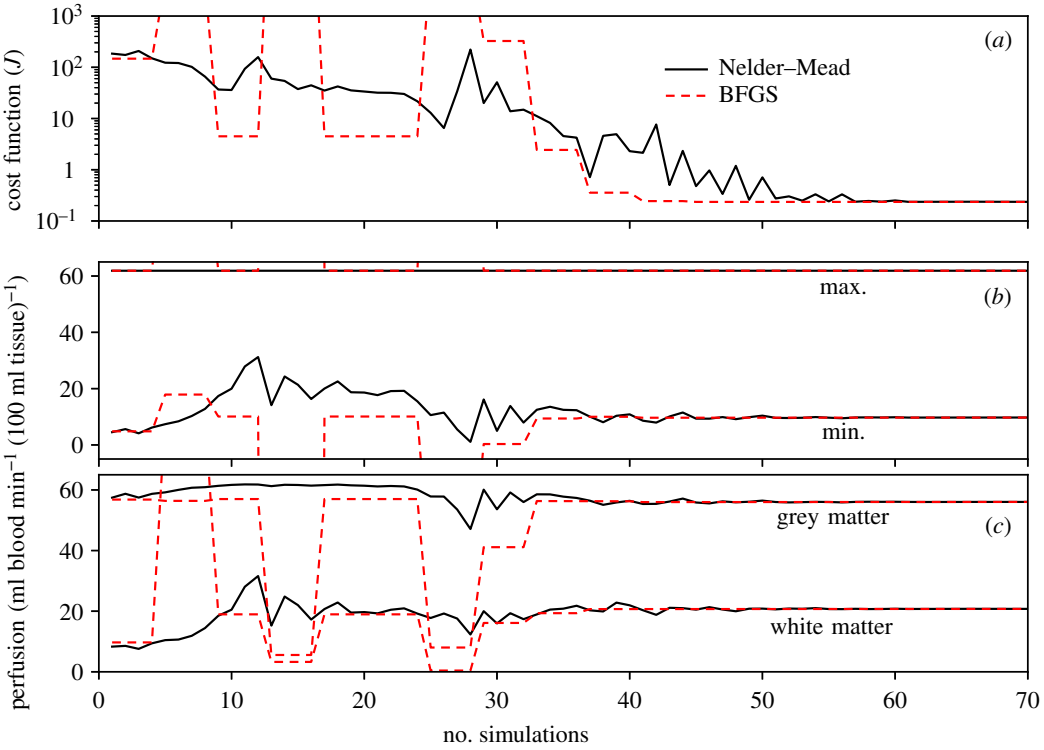

Figure 6. Convergence of the cost function J (*a*), minimum and maximum perfusion values (*b*), grey matter and white matter perfusion values (*c*) as functions of the number of simulations throughout the optimization.

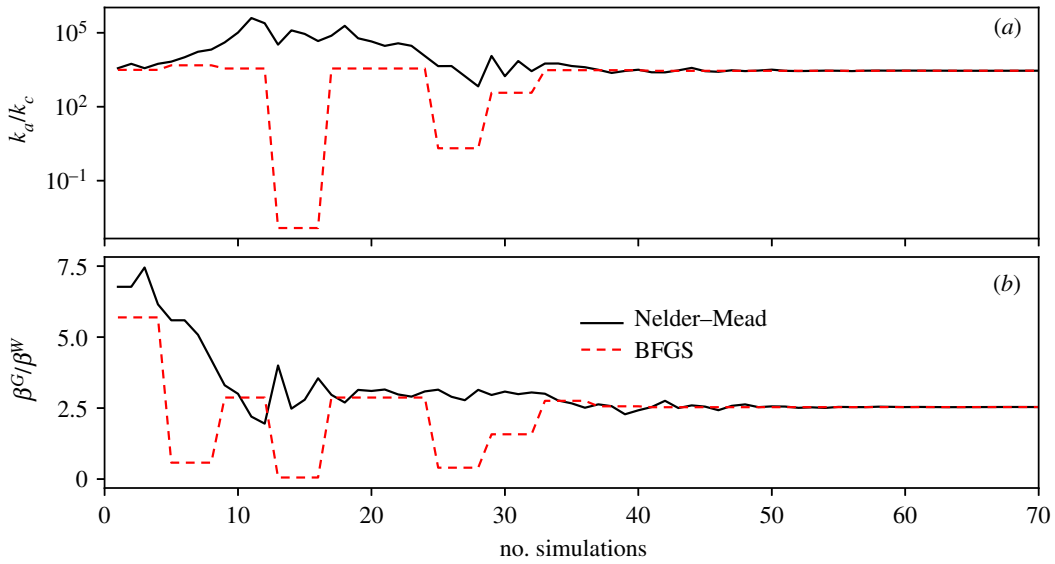

Figure 7. Convergence of the arteriole–capillary permeability ratio (*a*) and the coupling coefficient ratio (*b*) during the optimization.

the derivatives of the cost function, the Nelder–Mead algorithm is gradient-free.

Both algorithms are run three times so that the optimization problem is solved six times in total to ensure that the obtained parameters are independent of the initial guesses. Every run leads to the same values (with a relatively small tolerance) independently from the initialization. The cost function and the perfusion values during typical executions are shown in figure 6*a–c*. The methods converge to $J \approx 0.2$ within 60 simulations with the minimum, maximum and mean perfusion values reasonably close to the target values. The history of parameters throughout the optimization can be seen in figure 7. The final values of the simulation parameters are summarized in table 1.

3.2. Pressure and perfusion field analysis

Simulations are next performed to model a healthy scenario and a R-MCA occlusion. In order to evaluate the effects of anisotropic arterial and venule permeabilities, simulations are conducted for isotropic and anisotropic cases. The isotropic permeability tensors are set so that their Frobenius norms are equal to the norms of the anisotropic tensors resulting from the optimization described in §3.1. The pressure field corresponding to the healthy anisotropic scenario is displayed in figure 8. A high pressure drop can be observed in the vicinity of the cortical surface in the arteriole compartment which decreases rapidly as white matter is reached. The majority of the pressure drop takes place in the arteriole compartment

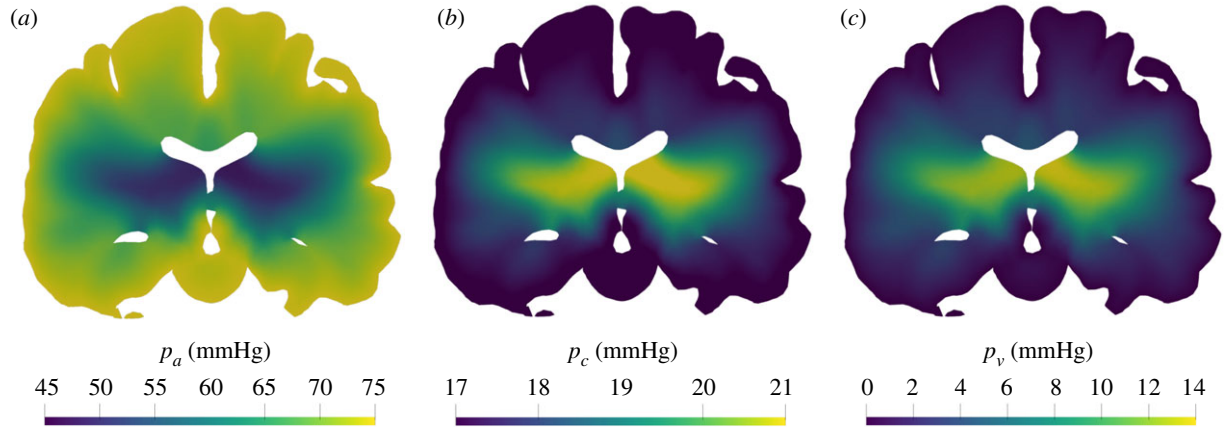

Figure 8. Pressure distribution corresponding to simulation with anisotropic permeabilities along the coronal plane shown in figure 2*c*: (*a*) arteriole, (*b*) capillary, (*c*) venule compartment.

Table 1. List of the model parameters.

parameter	value	unit
k_a	1.234	$mm^3\ s\ kg^{-1}$
k_c [19]	4.28×10^{-4}	$mm^3\ s\ kg^{-1}$
k_v	2.468	$mm^3\ s\ kg^{-1}$
β^G_{ac}	1.326×10^{-6}	$Pa^{-1}\ s^{-1}$
β^G_{cv}	4.641×10^{-6}	$Pa^{-1}\ s^{-1}$
β^W_{ac}	5.22×10^{-7}	$Pa^{-1}\ s^{-1}$
β^W_{cv}	1.828×10^{-6}	$Pa^{-1}\ s^{-1}$
p_v	0	Pa
p_{dia}	10^4 (75)	Pa (mmHg)

and between the arteriole and the capillary compartments. The pressure changes within the capillary and the venule compartments are relatively small. The volume-averaged pressure values listed in table 2 suggest that the pressure fields predicted by simulations with isotropic and anisotropic permeabilities are statistically similar.

The volume-averaged perfusion values are listed in table 2. Thanks to the optimization, the basic statistics extracted from the obtained perfusion field are in good agreement with ASL MRI data [32,56]. Since it has been recognized that obtaining the absolute value of perfusion from ASL MRI is cumbersome, we also considered positron emission tomography measurements [42]. Perfusion values in the healthy scenario are relatively low and hence the simulation is representative of an elderly male patient. Table 2 suggests that the proposed optimization method is suitable to determine model parameters so that the resulting perfusion is physiologically realistic compared to measurements in the healthy human brain. The simulation with isotropic permeability fields is statistically very similar to the anisotropic case.

The perfusion distribution within the brain in the healthy anisotropic scenario is visualized in figure 9. Perfusion distributions within the grey and white matters are approximately uniform as indicated by the standard deviation values in table 2. The standard deviation of perfusion within the brain is somewhat higher than the reference values. The difference is probably due to the fact that the simulation values

Table 2. Comparison of integral variables with literature data in the healthy scenario. The units of pressure and perfusion values are Pa and (ml blood) min^{-1} (100 ml tissue)$^{-1}$, respectively. Reference pressure is calculated from experimental data on the rat brain as presented in figure 5. Perfusion is listed as mean ± s.d. Standard deviations computed for the simulations describe spatial variation within the virtual brain. The standard deviations corresponding to the reference values represent variations between individuals.

	healthy		healthy reference	
variable	isotropic	anisotropic	female	male
$\langle p_a \rangle$	9035	9242	6335 [59]	
$\langle p_c \rangle$	2383	2348	1564 [58]	
$\langle p_v \rangle$	483	379	179 [58]	
F^{brain}	42 ± 18	43 ± 18	62 ± 7 [56]	53 ± 10 [56]
F^G	55 ± 7	56 ± 7	68 ± 10 [56]	58 ± 13 [56]
F^W	19 ± 2	21 ± 3	25 ± 5 [56]	23 ± 3 [56]

correspond to a spatial integration whereas the standard deviations of experimental values quantify the difference between patients. It is important to emphasize that the model is steady state. For this reason, spatial variations typical of the grey matter due to time-dependent activations are not visible.

Tissue perfusion is analysed following the occlusion of the M1-segment of the right middle cerebral artery because it accounts for more than 60% of ischaemic stroke cases [3,72]. Perfusion change is defined as

$$\text{perfusion change} = 100\% \left(\frac{F_{\text{occluded}} - F_{\text{healthy}}}{F_{\text{healty}}} \right), \qquad (3.5)$$

so that 0% stands for unchanged perfusion and −100% highlights regions with zero perfusion. Recently, computed tomography perfusion imaging has been used to estimate ischaemic regions based on a perfusion change threshold of −70% [73,74]. (It is worth noting that it has been reported that this approach overestimates the ischaemic region compared to diffusion-weighted magnetic resonance imaging [75].) The occluded scenario is modelled by setting blood flow to zero through the pial surface region corresponding to the right middle cerebral artery ($\partial p_a / \partial \boldsymbol{n} = 0$ at $\Gamma_{\text{R-MCA}}$).

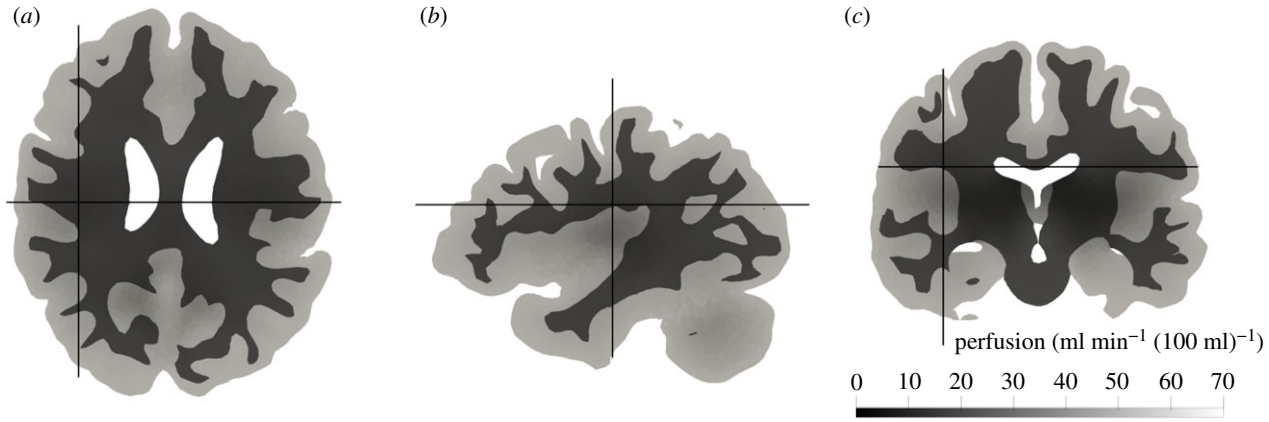

Figure 9. Perfusion distribution corresponding to simulation with anisotropic permeabilities along the transverse (*a*), sagittal (*b*) and coronal (*c*) planes shown in figure 2*c*. The solid lines show the location of the slices.

The modified boundary conditions are governed by equation (2.6). In order to evaluate the effects of anisotropic permeability fields, simulations have been conducted with isotropic and anisotropic permeabilities.

An underperfused region predicted by the isotropic and anisotropic models covering a significant part of the right hemisphere can be seen in figure 10*a–c* and 10*d–f*, respectively. The perfusion lesion in both cases diffuses towards deeper cerebral regions from $\Gamma_{\text{R-MCA}}$ because blood flow rate is set to zero through this territory. This feature underlines the importance of perfusion territory mapping based on VE ASL MRI and the role of model parameter optimization, which uniquely determine the origin and the extent of the lesion, respectively. Blood flows in the left hemisphere and the cerebellum are not influenced because these regions are perfused by different arteries. Although the human vasculature has compensatory mechanisms and structures to improve survival chance in the case of stroke, for example collateral arteries, it should be noted that these are not included in the model. Therefore, the simulations are capable of predicting only worse case scenarios for now. Collateral flow is often associated with leptomeningeal arteries with relatively large diameters; therefore, this feature could be included in the network model encapsulating the large arteries [15,16], even though the details of these vessels remain to be explored.

Comparing figure 10*a–c* to 10*d–f* leads to the conclusion that using isotropic permeabilities underestimates perfusion drop caused by a major cerebral artery occlusion. The results summarized in table 3 further emphasize the differences between simulations with isotropic and anisotropic permeability fields even though the two cases lead to statistically similar results in the healthy case (table 2). The isotropic model predicts that treatment is not required based on the −70% perfusion change threshold [73,74] because the isotropic permeability fields redistribute blood from other areas. By comparison, the same threshold leads to a lesion with significantly lower perfusion when anisotropic permeabilities are used. The anisotropic result suggests that the strongly interconnected capillary vessels cannot balance such a drastic loss of blood inflow due to their high resistance. Therefore, a relatively larger pressure drop is measured in the arteriole compartment of the anisotropic model as shown in tables 2 and 3. Since perfusion is $F = \beta_{\text{ac}}(p_a - p_c)$, this lower arterial pressure directly leads to decreased perfusion.

In figure 10*g–i*, follow-up non-contrast computed tomography (CT) scan images of a 76-year-old-male patient are presented one week after MCA stroke treatment. This patients have been selected for a brief, demonstrative validation because the noise level of the CT scan is low and hence a severe hypodensity of the right MCA territory associated with an acute infarct is clearly visible. Due to the late treatment resulting in poor recanalization (details in appendix C), it is reasonable to assume that the location and the extent of the infarct correlate well with the initial perfusion lesion. For simplicity, we follow the idea of perfusion-based ischaemic region estimation [73,74] and approximate the infarcted volume from simulations as the region where perfusion change is below −70%. Bearing in mind that this is a preliminary solution applicable only for virtual patients without or with unsuccessful treatment, the infarcted volume can be computed from figure 10*d–f* and figure 10*d–f* and 10*g–i* can be compared.

Non-contrast CT scans similar to figure 10*g–i* are used regularly to estimate the infarcted volume as an indicator of treatment outcome [76]. The infarcted volume measured for this patient is 309 ml. The model with anisotropic permeabilities predicts an infarcted volume of 238 ml based on the perfusion lesion. The simulation result is comparable to 134 ± 93 ml [77] and 138 ± 106 ml [76] measured in acute ischaemic stroke patients. The hypodense region in figure 10*g–i* is in satisfactory qualitative agreement with the low perfusion regions in figure 10*d–f*. The results suggest that produced virtual perfusion maps are qualitatively and quantitatively realistic. Even though the formation and expansion of an infarction core are clearly linked to the lack of perfusion, necrosis is driven by the lack of nutritions in general. Tissue metabolism relies on oxygen and glucose; therefore, it is essential to capture the advective–diffusive transport of these substances when it comes to the accurate prediction of the infarct volume. In order to provide estimation of ischaemic and infarcted regions, simulations similar to the ones presented herein will be fed into oxygen-transport [78] and metabolism [79,80] models predicting permanent tissue damage.

3.3. Limitations

This subsection aims to summarize some factors which have been overlooked in the present study. Firstly, fast, reliable and accurate automatized patient-specific mesh generation

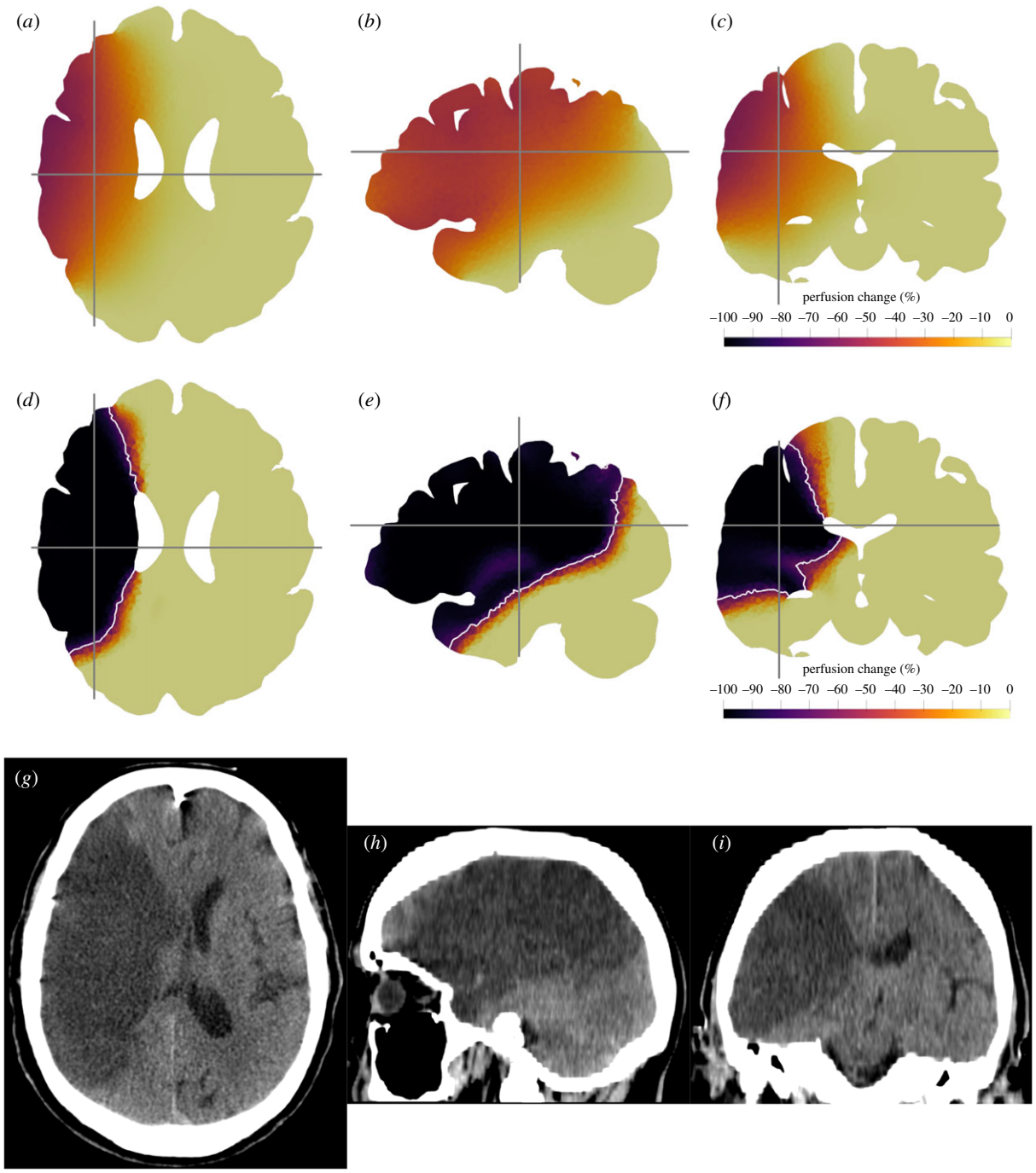

Figure 10. Relative change of perfusion as a result of a total blockage of the right middle cerebral artery (R-MCA) based on simulations with isotropic (*a–c*) and anisotropic (*d–f*) permeability fields. The grey solid lines show the location of the slices. The white isolines in (*d–f*) correspond to −70% perfusion change. (*g–i*) Non-contrast CT images of a patient showing an infarct caused by R-MCA occlusion. Transverse (*a*,*d*,*g*), sagittal (*b*,*e*,*h*) and coronal (*c*,*f*,*i*) planes.

remains a major challenge. For this reason, the present study is limited to a single patient-specific geometry. Organ-scale models have a great potential to ease clinical decision making and improve treatment but user-friendly and automatized pipelines need to be implemented. One of the major stumbling blocks of automatization is patient-specific mesh generation based on medical images.

Secondly, the presented multi-compartment porous model relies on multiple scale separation. It has been pointed out that the vessel diameter in the vasculature changes continuously therefore the applicability of scale separation is questionable [21]. The present study demonstrated promising but solely qualitative validation of this approach using medical images. The next stage of validation is to conduct a large set of simulations and evaluate the accuracy of predictions in comparison to medical images.

Thirdly, estimating the parameters of human physiological models has always been a difficult task because of the lack of sufficient data. The present optimization relies on numerous simplifications listed in §2. These assumptions have been used previously [23] and are sufficient to test models but they have not been thoroughly justified. Providing a more careful evaluation of the permeabilies and coupling coefficients in the grey matter based on statistically accurate network models of the microcirculation [19,51,53] is work in progress.

Finally, the following features have been neglected: cerebral autoregulation [47], cerebral oedema [11], emboli advection and blockage of the microcirculation [9,10], spreading of

Table 3. Comparison of integral variables obtained with isotropic and anisotropic permeabilities in the case of R-MCA occlusion. The units of pressure and perfusion values are Pa and (ml blood) min^{-1} (100 ml tissue)$^{-1}$, respectively. Standard deviations computed for the simulations describe spatial variation within the virtual brain.

	R-MCA occlusion	
variable	isotropic	anisotropic
$\langle p_a \rangle$	8263	7505
$\langle p_c \rangle$	2180	1907
$\langle p_v \rangle$	442	307
F^{brain}	39 ± 18	35 ± 22
F^{G}	50 ± 11	46 ± 21
F^{W}	18 ± 4	17 ± 8

ischaemic tissue damage [79,80] etc. These phenomena are time-dependent and often rely on nonlinear processes. Modelling these features and capturing their interaction could provide valuable new insights but due to their extreme complexity their description is beyond the scope of the present study. Nevertheless, it is worth recognizing that all of these features have a strong connection to cerebral blood flow. Therefore, the authors hope that the work presented herein will become a useful element of a comprehensive *in silico* human brain model that incorporates these neglected mechanisms.

4. Conclusion

This study has investigated the capabilities of a three-compartment porous microcirculation model for perfusion predictions in healthy humans as well as in ischaemic stroke patients. The governing equations have been discretized and solved using an open source finite-element library, FEniCS [65,66]. Inspired by advances in organ-scale human heart [28,60–62] and lung modelling [63,64], we aimed to lay down the fundamentals of a software suite which will facilitate a model environment for multi-scale and multi-physics simulations of the human brain.

An anatomically accurate mapping between large arteries and microvessels has been introduced. We have used VE-ASL MRI data and a novel clustering algorithm previously developed in our group to identify superficial cortical perfusion territories. A robust approach has been proposed to account for anisotropy in the microcirculation of the human brain using permeability tensors. To obtain the resulting parameters, optimization has been combined with parameter space reduction based on the analysis of the governing equations and experimental data.

For the first time, simulations have been conducted to predict perfusion in both healthy and occluded scenarios. A right middle cerebral artery occlusion has been implemented for which CT images of a patient with a proximal right MCA occlusion have also been presented. A satisfactory qualitative agreement has been found between the infarcted region visible in the CT images and the low perfusion region predicted by the simulations. Furthermore, the simulated perfusion lesion volume is comparable to clinical infarcted volume measurements. Identifying perfusion territories and obtaining anisotropic permeability fields appear to be crucial to provide such realistic predictions. In summary, porous microcirculation models are promising candidates to quantify the effects of stroke treatments on tissue perfusion and, with further extensions, on tissue health.

In the future, the model will be coupled to a one-dimensional network model of the large arteries [15,16] to create a complete *in silico* cerebral circulation model. Thereafter, the model will be validated using a large set of clinical data, such as CT perfusion images, which will also help to tune model parameters and improve accuracy. In order to predict infarct formation and propagation during ischaemic stroke, metabolism-based dynamic models will be developed.

Data accessibility. This article has no additional data.

Authors' contributions. T.I.J. has preprocessed the brain mesh, developed the finite-element models and the optimization of the model parameters, and written the manuscript under the supervision of S.J.P. R.M.P. has developed the brain territory clustering algorithm under the supervision of A.G.H. whereas N.S. prepared the patient's description and processed the corresponding CT image. T.I.J., W.K.E.-B., A.G.H. and S.J.P. have designed the research. Every author has contributed to the revision of the paper.

Competing interests. We declare we have no competing interests.

Funding. This work was funded by the European Union's Horizon 2020 research and innovation programme, the INSIST project, under grant agreement no. 777072.

Acknowledgements. Thanks are due to the members of the INSIST consortium for useful discussions and their sustained support. T.I.J. is grateful to H. J. M. M. Mutsaerts of Amsterdam UMC, T. W. Okell and M. A. Chappell of Universty of Oxford for sharing arterial spin labelling data and suggesting efficient application routes. T.I.J. also wishes to thank Patrick Farrell of University of Oxford for his insightful suggestions regarding parameter optimization.

Appendix A. Transformation matrix calculation

The permeability $\boldsymbol{K}_a^{\text{ref}}$ is given in the reference coordinate system defined by $\boldsymbol{e}_{\text{ref}}$ as detailed in §2.3.1. Furthermore, $\boldsymbol{e}_{\text{local}}$ is a vector field computed according to equations (2.11) and (2.10). The local permeability tensor is obtained from $\boldsymbol{K}_i = \boldsymbol{R}\boldsymbol{K}_i^{\text{ref}}\boldsymbol{R}^{\text{T}}$. Here, $\boldsymbol{R}$ is the transformation tensor which can be calculated as follows [81]. The unit vector defining the axis of rotation is

$$\boldsymbol{e}_{\text{rot}} = \frac{\boldsymbol{e}_{\text{ref}} \times \boldsymbol{e}_{\text{local}}}{|\boldsymbol{e}_{\text{ref}} \times \boldsymbol{e}_{\text{local}}|}. \tag{A 1}$$

The rotation angle θ can be calculated as $\cos^{-1}(\boldsymbol{e}_{\text{ref}} \cdot \boldsymbol{e}_{\text{local}})$ and the cross product matrix of $\boldsymbol{e}_{\text{rot}}$ is defined as

$$[\boldsymbol{e}_{\text{rot}}]_\times = \begin{bmatrix} 0 & -e_{\text{rot},3} & e_{\text{rot},2} \\ e_{\text{rot},3} & 0 & -e_{\text{rot},1} \\ -e_{\text{rot},2} & e_{\text{rot},1} & 0 \end{bmatrix}. \tag{A 2}$$

Here, $e_{\text{rot},i}$ is the ith component of $\boldsymbol{e}_{\text{rot}}$. Finally, the transformation matrix can be expressed as

$$\boldsymbol{R} = \cos(\theta)\boldsymbol{I} + \sin(\theta)[\boldsymbol{e}_{\text{rot}}]_\times + [1 - \cos(\theta)](\boldsymbol{e}_{\text{rot}} \otimes \boldsymbol{e}_{\text{rot}}), \tag{A 3}$$

where $\boldsymbol{I}$ denotes the identity matrix.

Appendix B. Weak form of the governing equations

The governing equation set and the imposed boundary conditions are equations (2.1) and (2.2)–(2.6), respectively. The weak form can be derived by taking the volume integral of equations (2.1*a*)–(2.1*b*). Thereafter, integration by parts and the application of the divergence theorem result in

$$\int_\Omega (\boldsymbol{K}_a \cdot \nabla p_a) \cdot (\nabla v_a)\,\mathrm{d}\Omega = -\int_\Omega \beta_{\mathrm{ac}}(p_a - p_c)v_a\,\mathrm{d}\Omega; \qquad (\mathrm{B}\,1a)$$

$$\int_\Omega (\boldsymbol{K}_c \cdot \nabla p_c) \cdot (\nabla v_c)\,\mathrm{d}\Omega = \int_\Omega \beta_{\mathrm{ac}}(p_a - p_c)v_c\,\mathrm{d}\Omega - \int_\Omega \beta_{\mathrm{cv}}(p_c - p_v)v_c\,\mathrm{d}\Omega; \qquad (\mathrm{B}\,1b)$$

$$\int_\Omega (\boldsymbol{K}_v \cdot \nabla p_v) \cdot (\nabla v_v)\mathrm{d}\Omega = \int_\Omega \beta_{\mathrm{cv}}(p_c - p_v)v_v\,\mathrm{d}\Omega. \qquad (\mathrm{B}\,1c)$$

In the above expression, v_i denotes the test function of compartment i.

Appendix C. The selected patient's case description

The patient arrived at the hospital four hours after stroke symptom onset. The CT angiography on hospital admission showed a proximal occlusion of the right M1-segment (mother branch) of the MCA and poor collaterals (only very few vessels visible in the occluded vascular territory compared to the asymptomatic contralateral hemisphere). The patient was diagnosed with a severe stroke-related neurologic deficit according to the National Institutes of Health Stroke scale. After diagnostic workup, the patient arrived at the angiosuite for thrombectomy approximately five hours after stroke onset. The treatment resulted in poor recanalization with modified thrombolysis in cerebral infarction (mTICI) score 1 meaning visible blood flow past the initial occlusion but no distal filling of the MCA territory. The mTICI score ranges from 0 (no recanalization) to 3 (complete recanalization) and successful treatment is usually defined as mTICI ≥ 2B [82].

References

1. Liebeskind DS. 2010 Reperfusion for acute ischemic stroke: arterial revascularization and collateral therapeutics. *Curr. Opin. Neurol.* **23**, 36–45. (doi:10.1097/WCO.0b013e328334da32)
2. Fransen PSS *et al.* 2014 MR CLEAN, a multicenter randomized clinical trial of endovascular treatment for acute ischemic stroke in The Netherlands: study protocol for a randomized controlled trial. *Trials* **15**, 343. (doi:10.1186/1745-6215-15-343)
3. Berkhemer OA *et al.* 2015 A randomized trial of intraarterial treatment for acute ischemic stroke. *N. Engl. J. Med.* **372**, 11–20. (doi:10.1056/NEJMoa1411587)
4. Goyal M *et al.* 2016 Endovascular thrombectomy after large-vessel ischaemic stroke: a meta-analysis of individual patient data from five randomised trials. *Lancet* **387**, 1723–1731. (doi:10.1016/S0140-6736(16)00163-X)
5. Seminog OO, Scarborough P, Wright FL, Rayner M, Goldacre MJ. 2019 Determinants of the decline in mortality from acute stroke in England: linked national database study of 795 869 adults. *Br. Med. J.* **365**, l1778. (doi:10.1136/bmj.l1778)
6. Dalkara T, Arsava EM. 2012 Can restoring incomplete microcirculatory reperfusion improve stroke outcome after thrombolysis? *J. Cereb. Blood Flow Metab.* **32**, 2091–2099. (doi:10.1038/jcbfm.2012.139)
7. Donkor ES. 2018 Stroke in the 21st century: a snapshot of the burden, epidemiology, and quality of life. *Stroke Res. Treat.* **2018**, 3238165. (doi:10.1155/2018/3238165)
8. Veerbeek JM, Kwakkel G, van Wegen EEH, Ket JCF, Heymans MW. 2011 Early prediction of outcome of activities of daily living after stroke: a systematic review. *Stroke* **42**, 1482–1488. (doi:10.1161/STROKEAHA.110.604090)
9. Marder VJ *et al.* 2006 Analysis of thrombi retrieved from cerebral arteries of patients with acute ischemic stroke. *Stroke* **37**, 2086–2093. (doi:10.1161/01.STR.0000230307.03438.94)
10. Bajd F, Sersa I. 2013 Mathematical modeling of blood clot fragmentation during flow-mediated thrombolysis. *Biophys. J.* **104**, 1181–1190. (doi:10.1016/j.bpj.2013.01.029)
11. Vardakis JC, Chou D, Tully BJ, Hung CC, Lee TH, Tsui P-H, Ventikos Y. 2016 Investigating cerebral oedema using poroelasticity. *Med. Eng. Phys.* **38**, 48–57. (doi:10.1016/j.medengphy.2015.09.006)
12. Gladstone DJ, Black SE, Hakim AM. 2002 Toward wisdom from failure—lessons from neuroprotective stroke trials and new therapeutic directions. *Stroke* **33**, 2123–2136. (doi:10.1161/01.STR.0000025518.34157.51)
13. Konduri PR *et al.* 2020 *In silico* trials for treatment of acute ischemic stroke. *Front. Neurol.* **11**, 558125. (doi:10.3389/fneur.2020.558125)
14. Hoekstra AG, van Bavel E, Siebes M, Gijsen F, Geris L. 2016 Virtual physiological human 2016: translating the virtual physiological human to the clinic. *Interface Focus* **8**, 20170067. (doi:10.1098/rsfs.2017.0067)
15. Padmos RM, Józsa TI, El-Bouri WK, Payne SJ, Hoekstra AG. 2019 Connecting arterial blood flow to tissue perfusion for in silico trials of acute ischaemic stroke. In *CompBioMed Conf., London, UK, 25–27 September 2019*.
16. Padmos RM, Józsa TI, El-Bouri WK, Konduri PR, Payne SJ, Hoekstra AG. 2021 Coupling one-dimensional arterial blood flow to three-dimensional tissue perfusion models for *in silico* trials of acute ischaemic stroke. *Interface Focus* **11**, 20190125. (doi:10.1098/rsfs.2019.0125)
17. Iadecola C. 2017 The neurovascular unit coming of age: a journey through neurovascular coupling in health and disease. *Neuron* **96**, 17–42. (doi:10.1016/j.neuron.2017.07.030)
18. Cassot F, Lauwers F, Fouard C, Prohaska S, Lauwers-Cances V. 2006 A novel three-dimensional computer-assisted method for a quantitative study of microvascular networks of the human cerebral cortex. *Microcirculation* **13**, 1–18. (doi:10.1080/10739680500383407)
19. El-Bouri WK, Payne SJ. 2015 Multi-scale homogenization of blood flow in 3-dimensional human cerebral microvascular networks. *J. Theor. Biol.* **380**, 40–47. (doi:10.1016/j.jtbi.2015.05.011)
20. El-Bouri WK, Payne SJ. 2018 Investigating the effects of a penetrating vessel occlusion with a multi-scale microvasculature model of the human cerebral cortex. *NeuroImage* **172**, 94–106. (doi:10.1016/j.neuroimage.2018.01.049)
21. Peyrounette M, Davit Y, Quintard M, Lorthois S. 2018 Multiscale modelling of blood flow in cerebral microcirculation: details at capillary scale control accuracy at the level of the cortex. *PLoS ONE* **13**, e0189474. (doi:10.1371/journal.pone.0189474)
22. Blowers S, Marshall I, Thrippleton M, Andrews P, Harris B, Bethune I, Valluri P. 2018 How does blood regulate cerebral temperatures during hypothermia? *Sci. Rep.* **8**, 7877. (doi:10.1038/s41598-018-26063-7)
23. Hodneland E *et al.* 2019 A new framework for assessing subject-specific whole brain circulation and perfusion using MRI-based measurements and a multi-scale continuous flow model. *PLoS Comput. Biol.* **15**, e1007073. (doi:10.1371/journal.pcbi.1007073)
24. Michler C *et al.* 2013 A computationally efficient framework for the simulation of cardiac perfusion using a multi-compartment Darcy porous-media flow model. *Int. J. Numer. Methods Biomed. Eng.* **29**, 217–232. (doi:10.1002/cnm.2520)
25. Hyde ER, Michler C, Lee J, Cookson AN, Chabiniok R, Nordsletten DA, Smith NP. 2013 Parameterisation of multi-scale continuum perfusion models from discrete vascular networks. *Med. Biol. Eng. Comput.* **51**, 557–570. (doi:10.1007/s11517-012-1025-2)

26. Hyde ER *et al.* 2014 Multi-scale parameterisation of a myocardial perfusion model using whole-organ arterial networks. *Ann. Biomed. Eng.* **42**, 797–811. (doi:10.1007/s10439-013-0951-y)
27. Guo L *et al.* 2018 Subject-specific multi-poroelastic model for exploring the risk factors associated with the early stages of Alzheimer's disease. *Interface Focus* **8**, 20170019. (doi:10.1098/rsfs.2017.0019)
28. Santiago A, Aguado-Sierra J, Zavala-Aké M, Doste-Beltran R, Gómez S, Arís R, Cajas JC, Casoni E, Vázquez M. 2018 Fully coupled fluid-electro-mechanical model of the human heart for supercomputers. *Int. J. Numer. Methods Biomed. Eng.* **34**, e3140. (doi:10.1002/cnm.3140)
29. Weickenmeier J, Jucker M, Goriely A, Kuhl E. 2019 A physics-based model explains the prion-like features of neurodegeneration in Alzheimer's disease, Parkinson's disease, and amyotrophic lateral sclerosis. *J. Mech. Phys. Solids* **124**, 264–281. (doi:10.1016/j.jmps.2018.10.013)
30. Tatu L, Moulin T, Bogousslavsky J, Duvernoy H. 1998 Arterial territories of the human brain: cerebral hemispheres. *Neurology* **50**, 1699–1708. (doi:10.1212/WNL.50.6.1699)
31. Okell TW, Chappell MA, Kelly ME, Jezzard P. 2013 Cerebral blood flow quantification using vessel-encoded arterial spin labeling. *J. Cereb. Blood Flow Metab.* **33**, 1716–1724. (doi:10.1038/jcbfm.2013.129)
32. Mutsaerts HJMM, van Dalen JW, Heijtel DFR, Groot PFC, Majoie CBLM, Petersen ET, Richard E, Nederveen AJ. 2015 Cerebral perfusion measurements in elderly with hypertension using arterial spin labeling. *PLoS ONE* **10**, e0133717. (doi:10.1371/journal.pone.0133717)
33. Alastruey J, Parker KH, Peiró J, Byrd SM, Sherwin SJ. 2007 Modelling the circle of Willis to assess the effects of anatomical variations and occlusions on cerebral flows. *J. Biomech.* **40**, 1794–1805. (doi:10.1016/j.jbiomech.2006.07.008)
34. Matthys KS, Alastruey J, Peiró J, Khir AW, Segers P, Verdonck PR, Parker KH, Sherwin SJ. 2007 Pulse wave propagation in a model human arterial network: assessment of 1-D numerical simulations against *in vitro* measurements. *J. Biomech.* **40**, 3476–3486. (doi:10.1016/j.jbiomech.2007.05.027)
35. Bárdossy G, Halász G. 2013 A 'backward' calculation method for the estimation of central aortic pressure wave in a 1D arterial model network. *Comput. Fluids* **73**, 134–144. (doi:10.1016/j.compfluid.2012.12.014)
36. Józsa T, Paál Gy. 2014 Boundary conditions for flow simulations of abdominal aortic aneurysms. *Int. J. Heat Fluid Flow* **50**, 342–351. (doi:10.1016/j.ijheatfluidflow.2014.09.004)
37. Blanco PJ, Müller LO, Spence JD. 2017 Blood pressure gradients in cerebral arteries: a clue to pathogenesis of cerebral small vessel disease. *Stroke Vasc. Neurol.* **2**, 108–117. (doi:10.1136/svn-2017-000087)
38. Garcia-Gonzalez D, Jayamohan J, Sotiropoulos SN, Yoon S-H, Cook J, Siviour CR, Arias A, Jérusalem A. 2017 On the mechanical behaviour of PEEK and HA cranial implants under impact loading. *J. Mech. Behav. Biomed. Mater.* **69**, 342–354. (doi:10.1016/j.jmbbm.2017.01.012)
39. Garcia-Gonzalez D *et al.* 2018 Cognition based bTBI mechanistic criteria; a tool for preventive and therapeutic innovations. *Sci. Rep.* **8**, 10273. (doi:10.1038/s41598-018-28271-7)
40. Si H. 2015 TetGen, a Delaunay-based quality tetrahedral mesh generator. *ACM Trans. Math. Softw.* **41**, 11. (doi:10.1145/2629697)
41. Hartkamp NS, Petersen ET, De Vis JB, Bokkers RPH, Hendrikse J. 2013 Mapping of cerebral perfusion territories using territorial arterial spin labeling: techniques and clinical application. *NMR Biomed.* **26**, 901–912. (doi:10.1002/nbm.2836)
42. Heijtel DFR*et al.* 2014 Accuracy and precision of pseudo-continuous arterial spin labeling perfusion during baseline and hypercapnia: a head-to-head comparison with ^{15}O H_2O positron emission tomography. *NeuroImage* **92**, 182–192. (doi:10.1016/j.neuroimage.2014.02.011)
43. Hartkamp NS, Petersen ET, Chappell MA, Okell TW, Uyttenboogaart M, Zeebregts CJ, Bokkers RPH. 2018 Relationship between haemodynamic impairment and collateral blood flow in carotid artery disease. *J. Cereb. Blood Flow Metab.* **38**, 2021–2032. (doi:10.1177/0271678X17724027)
44. Józsa TI, El-Bouri WK, Padmos RM, Payne SJ, Hoekstra AG. 2019 A cerebral circulation model for in silico clinical trials of ischaemic stroke. In *CompBioMed Conf., London, UK, 25–27 September 2019*.
45. Hill RA, Tong L, Yuan P, Murikinati S, Gupta S, Grutzendler J. 2015 Regional blood flow in the normal and ischemic brain is controlled by arteriolar smooth muscle cell contractility and not by capillary pericytes. *Neuron* **87**, 95–110. (doi:10.1016/j.neuron.2015.06.001)
46. Attwell D, Mishra A, Hall CN, O'Farrell FM, Dalkara T. 2016 What is a pericyte? *J. Cereb. Blood Flow Metab.* **36**, 451–455. (doi:10.1177/0271678X15610340)
47. Payne SJ 2017 *Cerebral blood flow and metabolism: a quantitative approach*. Singapore: World Scientific.
48. Schmid F, Tsai PS, Kleinfeld D, Jenny P, Weber B. 2017 Depth-dependent flow and pressure characteristics in cortical microvascular networks. *PLoS Comput. Biol.* **13**, e1005392. (doi:10.1371/journal.pcbi.1005392)
49. Duvernoy HM, Delon S, Vannson JL. 1981 Cortical blood vessels of the human brain. *Brain Res. Bull.* **7**, 519–579. (doi:10.1016/0361-9230(81)90007-1)
50. Smith AF *et al.* 2019 Brain capillary networks across species: a few simple organizational requirements are sufficient to reproduce both structure and function. *Front. Physiol.* **10**, 233. (doi:10.3389/fphys.2019.00233)
51. Su S-W, Catherall M, Payne SJ. 2012 The influence of network structure on the transport of blood in the human cerebral microvasculature. *Microcirculation* **19**, 175–187. (doi:10.1111/j.1549-8719.2011.00148.x)
52. Pries AR, Secomb TW, Gessner T, Sperandio MB, Gross JF, Gaehtgens P. 1994 Resistance to blood flow in microvessels *in vivo*. *Circ. Res.* **75**, 904–915. (doi:10.1161/01.RES.75.5.904)
53. El-Bouri WK, Payne SJ. 2016 A statistical model of the penetrating arterioles and venules in the human cerebral cortex. *Microcirculation* **23**, 580–590. (doi:10.1111/micc.12318)
54. Risser L, Plouraboue F, Cloetens P, Fonta C. 2009 A 3D-investigation shows that angiogenesis in primate cerebral cortex mainly occurs at capillary level. *Int. J. Dev. Neurosci.* **27**, 185–196. (doi:10.1016/j.ijdevneu.2008.10.006)
55. Xing C-Y, Tarumi T, Liu J, Zhang Y, Turner M, Riley J, Tinajero CD, Yuan L-J, Zhang R. 2017 Distribution of cardiac output to the brain across the adult lifespan. *J. Cereb. Blood Flow Metab.* **37**, 2848–2856. (doi:10.1177/0271678X16676826)
56. Parkes LM, Rashid W, Chard DT, Tofts PS. 2004 Normal cerebral perfusion measurements using arterial spin labeling: reproducibility, stability, and age and gender effects. *Magn. Reson. Med.* **51**, 736–743. (doi:10.1002/mrm.20023)
57. Lüders E, Steinmetz H, Jäncke L. 2002 Brain size and grey matter volume in the healthy human brain. *Neuroreport* **13**, 2371–2374. (doi:10.1097/00001756-200212030-00040)
58. Harper SL, Bohlen HG. 1984 Microvascular adaptation in the cerebral cortex of adult spontaneously hypertensive rats. *Hypertension* **6**, 408–419. (doi:10.1161/01.HYP.6.3.408)
59. Werber AH, Heistad DD. 1984 Effects of chronic hypertension and sympathetic nerves on the cerebral microvasculature of stroke-prone spontaneously hypertensive rats. *Circ. Res.* **55**, 286–294. (doi:10.1161/01.RES.55.3.286)
60. Relan J, Chinchapatnam P, Sermesant M, Rhode K, Ginks M, Delingette H, Rinaldi CA, Razavi R, Ayache N. 2011 Coupled personalization of cardiac electrophysiology models for prediction of ischaemic ventricular tachycardia. *Interface Focus* **1**, 396–407. (doi:10.1098/rsfs.2010.0041)
61. Vázquez M, Arís R, Houzeaux G, Aubry R, Villar P, Garcia-Barnés J, Gil D, Carreras F. 2011 A massively parallel computational electrophysiology model of the heart. *Int. J. Num. Methods Biomed. Eng.* **27**, 1911–1929. (doi:10.1002/cnm.1443)
62. Walmsley J, Rodriguez JF, Mirams GR, Burrage K, Efimov IR, Rodriguez B. 2013 mRNA expression levels in failing human hearts predict cellular electrophysiological remodeling: a population-based simulation study. *PLoS ONE* **8**, e56359. (doi:10.1371/journal.pone.0056359)
63. Burrowes KS *et al.* 2013 Multi-scale computational models of the airways to unravel the pathophysiological mechanisms in asthma and chronic obstructive pulmonary disease (AirPROM). *Interface Focus* **3**, 20120057. (doi:10.1098/rsfs.2012.0057)
64. Calmet H, Gambaruto AM, Bates AJ, Vázquez M, Houzeaux G, Doorly DJ. 2016 Large-scale CFD simulations of the transitional and turbulent regime

for the large human airways during rapid inhalation. *Comput. Biol. Med.* **69**, 166–180. (doi:10.1016/j.compbiomed.2015.12.003)

65. Logg A, Wells GN. 2010 DOLFIN: automated finite element computing. *ACM Trans. Math. Softw.* **37**, 20. (doi:10.1145/1731022.1731030)
66. Logg A, Mardal K-A, Wells G. 2012 *Automated solution of differential equations by the finite element method: the FEniCS book*, vol. 84. Berlin, Germany: Springer Science & Business Media.
67. Alnæs M, Blechta J, Hake J, Johansson A, Kehlet B, Logg A, Richardson C, Ring J, Rognes ME, Wells GN. 2015 The FEniCS project version 1.5. *Arch. Numer. Softw.* **3**, 9–23. (doi:10.11588/ans.2015.100.20553)
68. Van der Vorst HA. 1992 Bi-CGSTAB: a fast and smoothly converging variant of Bi-CG for the solution of nonsymmetric linear systems. *SIAM J. Sci. Stat. Comput.* **13**, 631–644. (doi:10.1137/0913035)
69. Shapira Y. 2003 Multigrid algorithms. In *Matrix-based multigrid*, pp. 61–67. New York, NY: Springer.
70. Zhu C, Byrd RH, Lu P, Nocedal J. 1997 Algorithm 778: L-BFGS-B: Fortran subroutines for large-scale bound-constrained optimization. *ACM Trans. Softw.* **23**, 550–560. (doi:10.1145/279232.279236)
71. Nelder JA, Mead R. 1965 A simplex method for function minimization. *Comput. J.* **7**, 308–313. (doi:10.1093/comjnl/7.4.308)
72. Compagne KCJ *et al.* 2019 Follow-up infarct volume as a mediator of endovascular treatment effect on functional outcome in ischaemic stroke. *Eur. Radiol.* **29**, 736–744. (doi:10.1007/s00330-018-5578-9)
73. Campbell BCV *et al.* 2015 Endovascular therapy for ischemic stroke with perfusion-imaging selection. *N. Engl. J. Med.* **372**, 1009–1018. (doi:10.1056/NEJMoa1414792)
74. Jovin TG *et al.* 2017 Diffusion-weighted imaging or computerized tomography perfusion assessment with clinical mismatch in the triage of wake up and late presenting strokes undergoing neurointervention with Trevo (DAWN) trial methods. *Int. J. Stroke* **12**, 641–652. (doi:10.1177/1747493017710341)
75. Copen WA, Yoo AJ, Rost NS, Morais LT, Schaefer PW, Gonzalez RG, Wu O. 2017 In patients with suspected acute stroke, CT perfusion-based cerebral blood flow maps cannot substitute for DWI in measuring the ischemic core. *PLoS ONE* **12**, e0188891. (doi:10.1371/journal.pone.0188891)
76. Boers AM, Marquering HA, Jochem JJ, Besselink NJ, Berkhemer OA, van der Lugt A, Beenen LF, Majoie CB. 2013 Automated cerebral infarct volume measurement in follow-up noncontrast CT scans of patients with acute ischemic stroke. *Am. J. Neuroradiol.* **34**, 1522–1527. (doi:10.3174/ajnr.A3463)
77. Pereira AC, Saunders DE, Doyle VL, Bland JM, Howe FA, Griffiths JR, Brown MM. 1999 Measurement of initial N-acetyl aspartate concentration by magnetic resonance spectroscopy and initial infarct volume by MRI predicts outcome in patients with middle cerebral artery territory infarction. *Stroke* **30**, 1577–1582. (doi:10.1161/01.STR.30.8.1577)
78. El-Bouri WK, Bing Y, Józsa TI, Payne SJ. 2019 A novel multi-scale, multi-compartment model of oxygen transport—towards in-silico clinical trials in the entire human brain. In *CompBioMed Conf., London, UK, 25–27 September 2019.*
79. Ruppin E, Ofer E, Reggia JA, Revett K, Goodall S. 1999 Pathogenic mechanisms in ischemic damage: a computational study. *Comput. Biol. Med.* **29**, 39–59. (doi:10.1016/S0010-4825(98)00044-4)
80. Vatov L, Kizner Z, Ruppin E, Meilin S, Manor T, Mayevsky A. 2006 Modeling brain energy metabolism and function: a multiparametric monitoring approach. *Bull. Math. Biol.* **68**, 275–291. (doi:10.1007/s11538-005-9008-1)
81. Cole IR. 2015 Modelling CPV. PhD thesis, Loughborough University.
82. Dargazanli C *et al.* 2018 Modified thrombolysis in cerebral infarction 2C/thrombolysis in cerebral infarction 3 reperfusion should be the aim of mechanical thrombectomy: insights from the ASTER trial (Contact Aspiration Versus Stent Retriever for Successful Revascularization). *Stroke* **49**, 1189–1196. (doi:10.1161/STROKEAHA.118.020700)